Journal of Materials Chemistry A

RSC Publishing

PAPER

View Article Online
View Journal | View Issue

Cite this: J. Mater. Chem. A, 2013, 1, 2543

A microporous metal–organic framework assembled from an aromatic tetracarboxylate for H_2 purification†

Yabing He,[a] Shengchang Xiang,[b] Zhangjing Zhang,[b] Shunshun Xiong,[a] Chuande Wu,[c] Wei Zhou,[de] Taner Yildirim,[df] Rajamani Krishna*[g] and Banglin Chen*[a]

Received 26th November 2012
Accepted 11th December 2012

DOI: 10.1039/c2ta01260j

www.rsc.org/MaterialsA

A NbO-type metal–organic framework **UTSA-40** constructed from a novel aromatic tetracarboxylate has been synthesized and structurally characterized. With open metal sites, suitable pore spaces and a moderate BET surface area of 1630 $m^2\ g^{-1}$ for the recognition of CO_2 and CH_4, the activated **UTSA-40a** has the potential for use in H_2 purification processes conducted in fixed bed adsorbers, with higher productivities and lower regeneration costs than those obtained with conventionally used **NaX** and **LTA-5A** zeolites when operating at higher pressure. Furthermore, its regeneration cost is also lower than that of the examined MOFs **MgMOF-74** and **Cu-TDPAT** despite its lower productivity.

Introduction

Hydrogen, considered as the cleanest and sustainable energy source carrier, is mostly produced by steam reforming of methane (SMR) and subsequent water gas shift (WGS). This procedure yields a hydrogen-rich product stream with different impurities, which typically consists of 71–75% H_2, 15–20% CO_2, 4–7% CH_4, 1–4% CO, and a trace of H_2O. In order to obtain high-purity hydrogen for its practical utilization, these contaminants need to be removed. One of the well explored technologies for hydrogen purification is pressure swing adsorption (PSA). Over the past two decades, some traditional porous materials such as zeolites and activated carbon have been well investigated for their PSA purification of hydrogen.[1]

Porous metal–organic frameworks (MOFs) are a new type of very promising porous materials for gas separation because their pore sizes/curvatures can be tuned by selecting diverse metal-containing secondary building blocks (SBUs) and rich organic linkers to maximize the size-selective effects, and furthermore, their pore surfaces can be modified synthetically or post-synthetically to direct the differential interactions with gas molecules.[2] In fact, a few microporous metal–organic frameworks for very challenging separations of C_2H_2/C_2H_4 and C_3H_6/C_3H_8 have even been realized recently.[3]

Porous MOFs for hydrogen separation have been less explored. The examined porous MOFs **MgMOF-74** and **Cu-TDPAT** have very strong interactions with CO_2, which presumably lead to high regeneration energy cost.[4] It is expected that more extensive research on porous MOFs for hydrogen purification will realize some very promising materials not only exhibiting high separation capacities and selectivities, but also minimizing the regeneration costs. In order to secure high separation capacities, the desired MOF materials should have moderately high porosities and optimized pore sizes for their high storage capacities of CO_2 and CH_4. Among the diverse porous MOFs, those constructed from isophthalate-derived carboxylic acids are particularly interesting and important (Table S10†).[5,6] Indeed, a series of such porous MOFs have been targeted for their high CO_2 and CH_4 adsorption,[5b,5f–h,6i] providing the basis for their application on hydrogen purification. We plan to systematically evaluate this series of MOFs for gas storage and hydrogen purification, and thus to target some industrially useful porous MOF materials for these important applications. Recently, we developed a chiral aromatic-rich tetracarboxylate (H_4L, Scheme 1) in order to explore enantiopure MOFs for asymmetric catalysis.[7] We speculate that the usage of this new organic linker should also lead to some moderately highly porous MOFs for their gas storage and

[a]Department of Chemistry, University of Texas at San Antonio, One UTSA Circle, San Antonio, Texas 78249-0698, USA. E-mail: Banglin.Chen@utsa.edu; Fax: +1-210-458-7428

[b]Fujian Provincial Key Laboratory of Polymer Materials, Fujian Normal University, 3 Shangsan Road, Cangshang Region, Fuzhou 350007, China

[c]Department of Chemistry, Zhejiang University, Hangzhou 310027, China

[d]NIST Center for Neutron Research, Gaithersburg, Maryland 20899-6102, USA

[e]Department of Materials Science and Engineering, University of Maryland, College Park, Maryland 20742, USA

[f]Department of Materials Science and Engineering, University of Pennsylvania, Philadelphia, Pennsylvania 19104-6272, USA

[g]Van't Hoff Institute of Molecular Science, University of Amsterdam, Science Park 904, 1098 XH Amsterdam, The Netherlands. E-mail: r.krishna@uva.nl

† Electronic supplementary information (ESI) available: PXRD (Fig. S1); TGA (Fig. S2); BET and Langmuir plots (Fig. S3); high-pressure absolute and excess sorption isotherms (Fig. S4); FTIR (Fig. S5); NMR (Fig. S6); structural data of the different adsorbents evaluated in this study (Table S1); fit parameters for **UTSA-40a**, **MgMOF-74**, **Cu-TDPAT**, **MIL-101**, **NaX** and **LTA-5A** (Tables S2–S8); crystal data and structure refinement for **UTSA-40** (Table S9); gas sorption properties in reported porous copper–tetracarboxylate frameworks (Table S10). CCDC 896825. For ESI and crystallographic data in CIF or other electronic format see DOI: 10.1039/c2ta01260j

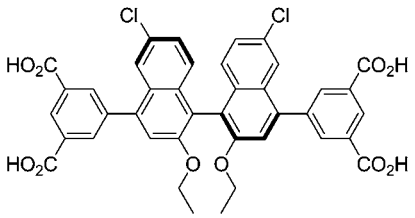

Scheme 1 The organic linker H_4L used to construct **UTSA-40**.

separation, particularly because the functional organic groups within this organic linker can optimize and/or tune the pores for their efficient uptake of gas molecules and for their sieving effects to enhance gas separation selectivity. Herein we report the synthesis, structure and hydrogen purification potential of the MOF $[Cu_2L(H_2O)_2]\cdot 6DMF\cdot 2H_2O$ (**UTSA-40**).

Experimental section

General procedures

All reagents and solvents were used as received from commercial suppliers without further purification. ^1H NMR and ^{13}C NMR spectra were recorded on a Varian Mercury 300 MHz or Bruker AV 600 MHz spectrometer. Tetramethylsilane (TMS) and deuterated solvents ($CDCl_3$, $\delta = 77.00$ ppm; DMSO-d_6, $\delta = 39.50$ ppm) were used as internal standards in ^1H NMR and ^{13}C NMR experiments, respectively. The coupling constants were reported in Hertz. FTIR spectra were recorded on a Bruker Vector 22 spectrometer at room temperature. The elemental analyses were performed with Perkin-Elmer 240 CHN analyzers from Galbraith Laboratories, Knoxville. Thermogravimetric analyses (TGA) were performed using a Shimadzu TGA-50 analyzer under a nitrogen atmosphere with a heating rate of 5 K min^{-1}. Powder X-ray diffraction (PXRD) patterns were recorded using a Rigaku Ultima IV diffractometer operated at 40 kV and 44 mA with a scan rate of 1.0 deg min^{-1}. A Micromeritics ASAP 2020 surface area analyzer was used to obtain N_2 sorption isotherms. To obtain a guest-free framework, the fresh sample was guest-exchanged with dry acetone at least 10 times, filtered and vacuumed at room temperature for 24 h and then at 383 K until the outgas rate was 5 μm Hg min^{-1} prior to measurements. A sample of 84.2 mg was used for the sorption measurements and was maintained at 77 K with liquid nitrogen. High-pressure CO_2, CH_4, and H_2 sorption isotherms were obtained using a computer controlled Sieverts-type apparatus, details of which have been published elsewhere.[8]

X-ray crystallography

The crystallographic measurement was performed on an Oxford Xcalibur Gemini Ultra diffractometer with an Atlas detector. The data were collected using graphite-monochromatic enhanced ultra Cu radiation ($\lambda = 1.54178$ Å) at 293 K. The datasets were corrected by empirical absorption correction using spherical harmonics, implemented in the SCALE3 ABSPACK scaling algorithm. The structure was solved by direct methods and refined by full matrix least-squares methods with the SHELX-97 program package. The solvent molecules in the compound are highly disordered. The SQUEEZE subroutine of the PLATON software suit was used to remove the scattering from the highly disordered guest molecules.[9] The resulting new files were used to further refine the structures. The H atoms on C atoms were generated geometrically. Crystal data for **UTSA-40**: trigonal, $R3_2$, $a = b = 18.5676(7)$ Å, $c = 52.205(3)$ Å, $V = 15\,586.8(12)$ Å^3, $Z = 9$, $D_c = 1.3165$ g cm^{-3}, $\mu = 1.750$ mm^{-1}, $R_1 = 0.0715$ for $I > 2\sigma(I)$, $wR_2 = 0.2237$ for all data. CCDC 896825.

Fitting of pure-component isotherms

The pure-component CO_2 adsorption isotherm data of **UTSA-40a**, covering both the low- and high-pressure ranges measured at three different temperatures (240 K, 270 K, and 300 K), were fitted with the dual-site Langmuir–Freundlich model

$$q = q_{A,sat}\frac{b_A p^{\nu_A}}{1 + b_A p^{\nu_A}} + q_{B,sat}\frac{b_B p^{\nu_B}}{1 + b_B p^{\nu_B}} \quad (1)$$

with T-dependent parameters b_A and b_B

$$b_A = b_{A0}\exp\left(\frac{E_A}{RT}\right); \quad b_B = b_{B0}\exp\left(\frac{E_B}{RT}\right) \quad (2)$$

The fit parameters are provided in Table S2.† The pure-component CH_4 and H_2 adsorption isotherms of **UTSA-40a** do not display any inflection characteristics, and therefore the single-site Langmuir model

$$q = \frac{q_{sat} bp}{1 + bp} \quad (3)$$

can provide an adequately good representation of the absolute loadings. The fit parameters are provided in Tables S2 and S3.†

For evaluating the performance of **MgMOF-74**, the pure-component CO_2 and CH_4 adsorption isotherm data were obtained from the works of Mason *et al.*,[10] Herm *et al.*,[4a,b] and Dietzel *et al.*[11] The measured experimental data of excess loadings were converted to absolute loadings for fitting purposes. The temperature-dependent fit parameters are specified in Table S4.† The pure-component H_2 adsorption isotherm data at 298 K have been reported by Yaghi in a document that is available on the Web.[12] The fit parameters are provided in Table S4.†

For evaluating the performance of **Cu-TDPAT**, the pure-component CO_2, CH_4, and H_2 adsorption isotherm data were obtained from the works of Wu *et al.*[4c] The fit parameters are provided in Table S5.†

For evaluating the performance of **MIL-101**, the pure-component CO_2 and CH_4 adsorption isotherm data were obtained from the works of Chowdhury *et al.*[13] The temperature-dependent fit parameters are specified in Table S6.† The pure-component H_2 adsorption isotherm data at 298 K were reported by Latroche *et al.*[14] These data were fitted with the Langmuir constants specified in Table S6.†

For evaluating the performance of zeolite **NaX**, we used the pure-component CO_2, CH_4, and H_2 adsorption isotherm data reported by Belmabkhout *et al.*[15] and Cavenati *et al.*[16] at various temperatures. The excess loadings reported in these papers are

converted to absolute loadings using a pore volume of 0.28 $cm^3 g^{-1}$, along with the Peng–Robinson equation of state for estimation of the fluid phase densities within the pores. The temperature-dependent fit parameters are specified in Table S7.†

Table S8† presents the dual-site Langmuir–Freundlich fit parameters for pure-component CO_2, CH_4, and H_2 adsorption isotherms of zeolite **LTA-5A**, which are derived from fitting the data presented in Table 1 in the paper by Pakseresht *et al.*,[17] along with Fig. 6 in the paper by Sircar and Golden.[18]

Isosteric heat of adsorption

The isosteric heat of adsorption, Q_{st}, defined as

$$Q_{st} = RT^2\left(\frac{\partial \ln p}{\partial T}\right)_q \quad (4)$$

was determined using the pure-component isotherm fits. The calculations of Q_{st} are based on the use of the Clausius–Clapeyron equation, using numerical procedures for differentiation of the dual-site Langmuir–Freundlich model.

Calculations of adsorption selectivity

The selectivity of preferential adsorption of component 1 over component 2 in a mixture containing 1 and 2, perhaps in the presence of other components too, can be formally defined as

$$S_{ads} = \frac{q_1/q_2}{p_1/p_2} \quad (5)$$

In eqn (5), q_1 and q_2 are the absolute loadings. In all the calculations to be presented below, the calculations of S_{ads} are based on the use of the Ideal Adsorbed Solution Theory (IAST) of Myers and Prausnitz.[19] These calculations are carried out using the pure-component isotherm fits of absolute loadings.

Packed bed adsorber breakthrough simulation methodology

Assuming plug flow of the gas mixture through the fixed bed maintained under isothermal conditions and negligible pressure drop, the partial pressures in the gas phase at any position and instant of time are obtained by solving the following set of partial differential equations for each of the species i in the gas mixture.

$$\frac{1}{RT}\frac{\partial p_i(t,z)}{\partial t} = -\frac{1}{RT}\frac{\partial (v(t,z)p_i(t,z))}{\partial z} - \frac{(1-\varepsilon)}{\varepsilon}\rho\frac{\partial q_i(t,z)}{\partial t}; \quad i = 1, 2, \ldots n \quad (6)$$

In eqn (6), t is the time, z is the distance along the adsorber, ρ is the framework density, ε is the bed voidage (ε = 1 − (bulk density)/(framework density)), and v is the interstitial gas velocity, equal to the superficial gas velocity, u, divided by ε. The adsorber bed is initially free of adsorbates, *i.e.* we have the initial conditions

$$t = 0;\ q_i(0,z) = 0 \quad (7)$$

At time $t = 0$, the inlet to the adsorber, $z = 0$, is subjected to a step input of the ternary gas mixture and this step input is maintained until the end of the adsorption cycle when steady-state conditions are reached.

$$t \geq 0;\ p_i(0,t) = p_{i0};\ v(0,t) = u_0/\varepsilon \quad (8)$$

where u_0 is the superficial gas velocity at the inlet to the adsorber. Invoking the constraint of negligible pressure drop, the overall material balance is obtained by summing eqn (6) over the three component species

$$\frac{1}{RT}p_t\frac{\partial (v(t,z))}{\partial z} = -\frac{(1-\varepsilon)}{\varepsilon}\rho\frac{\partial q_t(t,z)}{\partial t} \quad (9)$$

Eqn (9) allows the calculation of the interstitial gas velocity v along the length of the adsorber. For high-pressure separations considered in this work, the variation of the gas velocity along the length of the adsorber, and with time, needs to be properly accounted for. The molar loadings of the species i, $q_i(z,t)$ at any position z, and time t are determined from IAST calculations. Eqn (6) is first subjected to finite volume discretization. Typically, the adsorber length L is divided into 100 slices. Further details of the adsorber model, along with the numerical procedures used in this work, are provided in our earlier works.[3c,4c,20,21] The typical computation time for a binary gas mixture breakthrough is less than 100 s, allowing such transient adsorber calculations to be routinely used for screening purposes. Experimental validation of the breakthrough simulation methodology is available in the published literature.[3c,f,4c] The following parameter values were used: $L = 0.1$ m; $\varepsilon = 0.4$; $v = 0.1$ m s^{-1} (at the inlet). When comparing different materials, the fractional voidage is held constant at $\varepsilon = 0.4$. This implies that the volumes of adsorbents used in the fixed bed are the same for **UTSA-40a**, **MgMOF-74**, **Cu-TDPAT**, **MIL-101**, **LTA-5A**, and **NaX**. The total mass of the adsorbents used is governed by the framework density.

Synthesis and characterization of the organic linker H_4L

6,6′-Dichloro-2,2′-diethoxy-4,4′-di(3,5-bis(methoxycarbonyl)-phenyl)-2,2′-binaphthyl (H_4L-Me). To a degassed mixture of (*R*)-6,6′-dichloro-4,4′-dibromo-2,2′-diethoxy-1,1′-binaphthyl (2.00 g, 3.51 mmol), dimethyl 5-(pinacolboryl)isophthalate (2.31 g, 7.22 mmol), and anhydrous K_3PO_4 (7.46 g, 35.14 mmol) in dry dioxane (200 mL) was added $Pd(PPh_3)_4$ (203.10 mg, 0.18 mmol). The resulting mixture was refluxed for 72 h under a nitrogen atmosphere. After removal of the solvent, the residue was diluted with CH_2Cl_2 (100 mL) and water (80 mL). The organic phase was separated, and the aqueous phase was extracted with CH_2Cl_2 (50 mL × 2). The combined organic phase was washed with brine (40 mL × 2) and dried over anhydrous $MgSO_4$. After evaporation of the solvent, the residue was purified by silica gel column chromatography (*n*-hexane–ethyl acetate = 1/1, v/v) to give the desired compound as a pure white solid (2.04 g, 2.56 mmol) in 73% yield. ^{1}H NMR ($CDCl_3$, 600.1 MHz) δ (ppm): 8.837 (*t*, J = 1.8 Hz, 2H), 8.461 (d, J = 1.8 Hz, 4H), 7.650 (d, J = 1.8 Hz, 2H), 7.377 (s, 2H), 7.219 (dd, J = 9.0 Hz, 1.8 Hz, 2H), 7.183 (d, J = 9.0 Hz, 2H), 4.105 (m, 4H), 4.018 (s, 6H), 1.132 (*t*, J = 7.2 Hz, 6H); ^{13}C NMR ($CDCl_3$, 150.9 MHz) δ (ppm): 166.10, 153.83, 140.96,

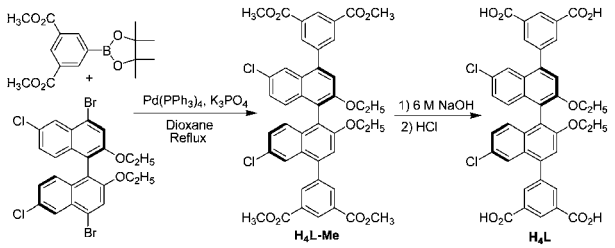

Scheme 2 Synthetic route to the organic linker H_4L.

138.86, 135.11, 132.76, 131.09, 130.15, 130.04, 127.85, 127.48, 127.41, 124.34, 120.12, 117.65, 65.25, 52.55, 14.99.

6,6′-Dichloro-2,2′-diethoxy-1,1′-binaphthyl-4,4′-di(5-isophthalic acid) (H_4L). To a methanol solution (20 mL) of 6,6′-dichloro-2,2′-diethoxy-4,4′-di(3,5-bis(methoxycarbonyl)phenyl)-2,2′-binaphthyl (1.50 g, 1.89 mmol) was added 6 M NaOH aqueous solution (10.0 mL, 60.0 mmol). The mixture was stirred under reflux for 8 h. Then HCl aqueous solution (10%, 30 mL) was added to the reaction mixture in an ice-water bath, which was stirred for an additional 1 h. The resultant precipitate was filtered and washed with H_2O (20 mL × 3). After being dried under vacuum, 1.37 g of organic building block (*R*)-H_4L was obtained as an off-white solid (98%) (Scheme 2). ^{1}H NMR (DMSO-d_6, 300.0 MHz) δ (ppm): 13.480 (s, br, 4H), 8.632 (*t*, J = 1.2 Hz, 2H), 8.345 (d, J = 1.2 Hz, 4H), 7.685 (s, 2H), 7.638 (d, J = 2.4 Hz, 2H), 7.347 (dd, J = 9.2 Hz, 2.4 Hz, 2H), 7.156 (d, J = 9.2 Hz, 2H), 4.200 (m, 4H), 1.050 (*t*, J = 7.6 Hz, 6H); ^{13}C NMR (DMSO-d_6, 75.4 MHz) δ (ppm): 166.41, 153.78, 139.93, 134.41, 132.31, 131.87, 129.36, 128.90, 127.69, 127.08, 127.04, 123.59, 119.00, 117.86, 64.47, 14.70; selected FTIR (neat, cm^{-1}): 1693, 1581, 1494, 1441, 1372, 1325, 1201, 1110, 1088, 1037, 910, 869, 816, 758, 714.

Synthesis and characterization of UTSA-40

A mixture of the organic linker H_4L (10.0 mg, 13.5 μmol) and $Cu(NO_3)_2\cdot 2.5H_2O$ (20.0 mg, 86.0 μmol, Aldrich) was dissolved into a mixed solvent (DMF–C_2H_5OH–H_2O, 1.5/0.5/0.2 mL) in a screw-capped vial (20 mL). 40 μL of 6 M HCl were then added. The vial was capped and heated at 363 K for 48 h. Greenish rhombic crystals were obtained in 45% yield. **UTSA-40** can be best formulated as $[Cu_2L(H_2O)_2]\cdot 6DMF\cdot 2H_2O$ on the basis of single-crystal X-ray structure determination, TGA and microanalysis. Selected FTIR (neat, cm^{-1}): 1654, 1624, 1580, 1492, 1418, 1367, 1338, 1244, 1205, 1143, 1088, 1056, 1014, 915, 871, 817, 776, 729, 717, 659; TGA data for loss of 6DMF and 4H_2O: calcd: 37.2%, found: 37.6%; anal. for $C_{58}H_{74}Cl_2Cu_2N_6O_{20}$: calcd: C 50.73, H 5.43, N 6.12, found: C 50.43, H 5.66, N 6.08%.

Results and discussion

Synthesis and characterization

The organic linker H_4L was readily synthesized by Suzuki cross-coupling of dimethyl 5-(pinacolboryl)isophthalate and 4,4′-dibromo-6,6′-dichloro-2,2′-diethoxy-1,1′-binaphthyl followed by hydrolysis and acidification. **UTSA-40** was obtained as greenish rhombic crystals *via* a solvothermal reaction of the organic linker H_4L and $Cu(NO_3)_2\cdot 2.5H_2O$ in the mixed solvents of *N*,*N*′-dimethylformamide (DMF)–C_2H_5OH–H_2O at 363 K under acidic conditions for 48 h. The structure was characterized by single-crystal X-ray diffraction, and the phase purity of the bulk material was confirmed by powder X-ray diffraction (PXRD, Fig. S1 in the ESI†). Based on the single-crystal structure determination, thermogravimetric analysis (TGA, Fig. S2 in the ESI†) and microanalysis, **UTSA-40** can be formulated as $[Cu_2(L)(H_2O)_2]\cdot 6DMF\cdot 2H_2O$. TGA under a nitrogen atmosphere reveals a weight loss of 37.6% up to 553 K, corresponding to the loss of free solvents and terminal water molecules (calcd 37.2%). Above this temperature, the complex starts to decompose rapidly.

Crystal structures

Single-crystal X-ray diffraction reveals that **UTSA-40** crystallizes in the chiral space group $R3_2$ due to the presence of the chiral binaphthyl groups in the organic linkers. As expected, the framework is composed of *in situ* formed square-planar dicopper paddle-wheel secondary building units (SBUs) which are bridged by the rectangular organic building blocks to form a three-dimensional noninterpenetrated NbO-type network (Fig. 1a and c). The dihedral angle between the two naphthalene rings in the 1,1′-binaphthyl subunit of the organic linker is 118.23°. The framework of **UTSA-40** contains two types of cavities (Fig. 1b). The pseudo octahedral cage consists of 12 ligands connecting 6 paddle-wheel SBUs. In this cage, each ligand utilizes two of its four carboxylate groups to support the cavity (Fig. 1b, yellow spheres). The irregular cage is formed from 6 ligands connecting 12 paddle-wheel SBUs. In this type, each ligand uses all of its four carboxylate groups to support the cavity (Fig. 1b, purple sphere). The two types of cavities are

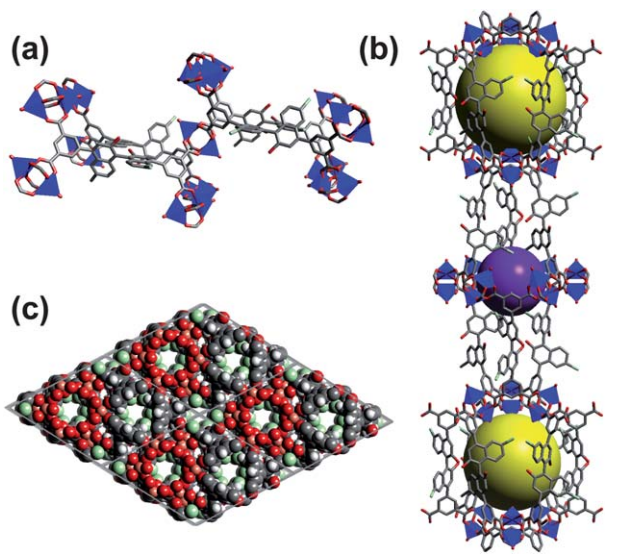

Fig. 1 Single-crystal X-ray structure of **UTSA-40**. (a) Each paddle-wheel $Cu_2(COO)_4$ unit connects with twelve such units by four organic linkers. The copper atoms are shown in polyhedra; (b) two types of cages: a pseudo octahedral cage (10 × 12 Å^2, yellow) and an irregular cage (6 × 11 Å^2, purple); and (c) CPK representation of a three-dimensional open framework viewed along the *c* direction. The hydrogen atoms and ethyl groups were omitted for clarity.

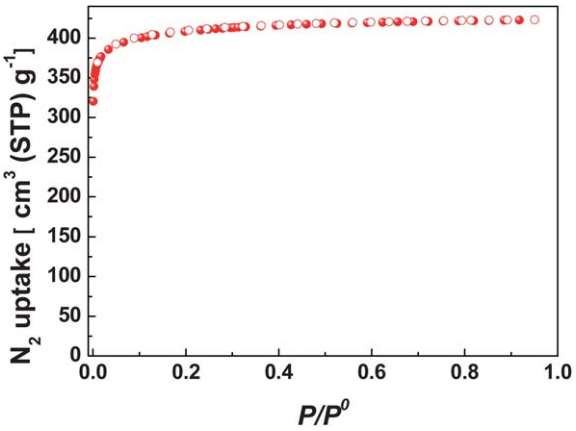

Fig. 2 N_2 sorption isotherm of **UTSA-40a** at 77 K. Filled and open symbols represent adsorption and desorption data, respectively.

connected to each other by sharing three paddle-wheel SBUs, and arranged in an alternating fashion. The accessible pore volume is 62.8% as calculated using the PLATON program after removal of all solvent molecules and coordinated water molecules.[9]

Permanent porosity

The permanent porosity was unambiguously established by the N_2 sorption isotherm at 77 K. Prior to gas sorption analysis, the as-prepared **UTSA-40** was solvent-exchanged with dry acetone and then evacuated at 383 K under high vacuum. The greenish crystalline samples turned dark blue during this process, indicating the removal of the terminal water molecules. The integrity of the framework was confirmed by powder X-ray diffraction (Fig. S1 in the ESI†). The nitrogen sorption isotherm reveals a typical reversible type-I sorption behaviour characteristic of microporous materials (Fig. 2). Brunauer–Emmett–Teller (BET) and Langmuir surface areas were estimated to be 1630 and 1662 $m^2\ g^{-1}$, respectively (Fig. S3 in the ESI†), and the pore volume calculated from the maximum amount of N_2 adsorbed is 0.65 $cm^3\ g^{-1}$. These values are comparable to those of **MOF-505** (ref. 6*a*) but lower than those of **NOTT-102.**[6b]

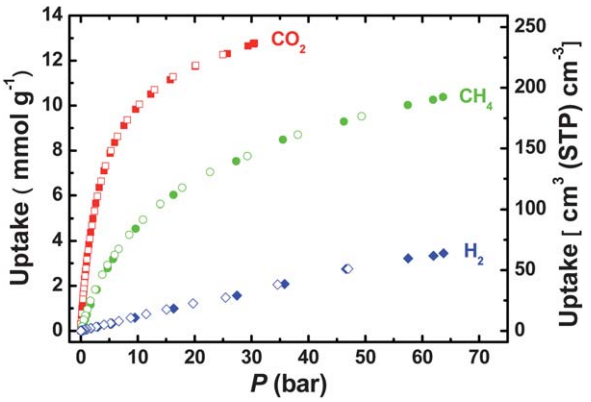

Fig. 3 High-pressure absolute CO_2, CH_4, and H_2 sorption isotherms of **UTSA-40a** at 300 K. Filled and open symbols represent adsorption and desorption data, respectively.

High-pressure sorption isotherms

To evaluate its potential for hydrogen purification, high-pressure CO_2, CH_4, and H_2 sorption isotherms of the activated **UTSA-40a** were measured at different temperatures using a volumetric measurement method (Fig. S4 in the ESI†), and the data at 300 K are presented in Fig. 3. The absolute H_2 uptake of **UTSA-40a** is 0.7% at 300 K and 60 bar, while **UTSA-40a** adsorbs CH_4 up to 13.4% (188 $cm^3\ cm^{-3}$, absolute) at 300 K and 60 bar, and CO_2 up to 55.9% (236 $cm^3\ cm^{-3}$, absolute) at 300 K and 30 bar. CO_2 and CH_4 adsorption capacities are much higher than the corresponding one for H_2, indicating that **UTSA-40a** can act as an efficient sorption material for selective adsorption of CO_2 and CH_4 from H_2.

IAST calculations

In order to establish the feasibility of this separation, we performed calculations using the Ideal Adsorbed Solution Theory (IAST) of Myers and Prausnitz.[19] The accuracy of IAST for

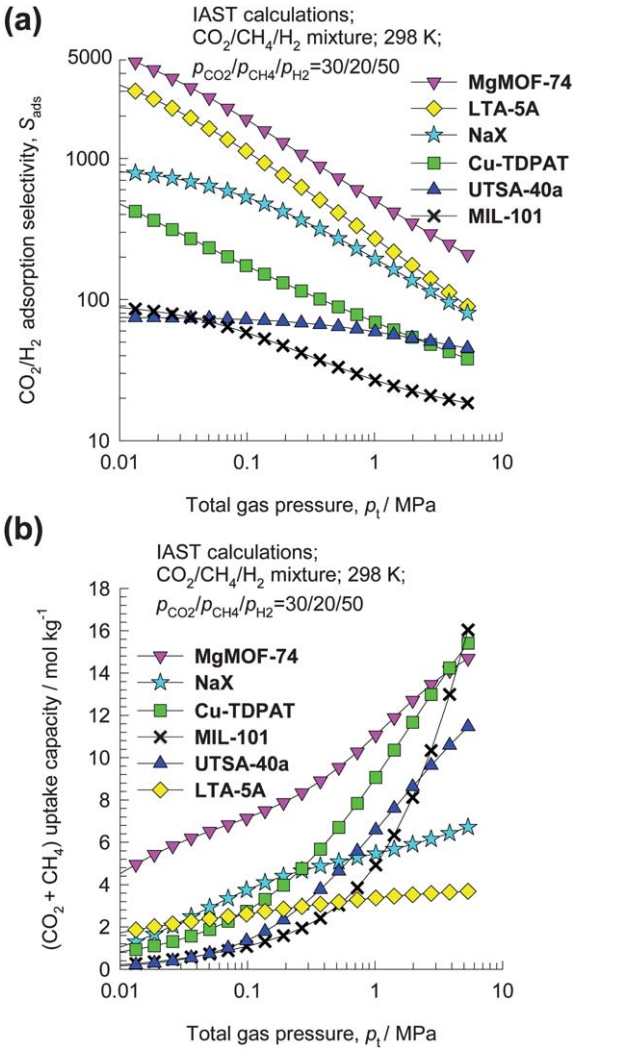

Fig. 4 IAST calculations of (a) CO_2/H_2 adsorption selectivity, and (b) the combined total CO_2 + CH_4 uptake capacity, in equilibrium with a 30/20/50 CO_2–CH_4–H_2 ternary mixture maintained under isothermal conditions at 298 K.

estimation of binary mixture equilibrium in zeolites and MOFs has been established in a number of publications in the literature.[20,22–24] Fig. 4a presents the IAST calculations of the CO_2/H_2 adsorption selectivity in a 30/20/50 CO_2–CH_4–H_2 ternary gas mixture. The gas composition was deliberately chosen to contain the maximum level of impurities CO_2 and CH_4 that are likely to be encountered in industrial practice. For comparison, the traditionally used zeolites **NaX**[15,16] and **LTA-5A**[17,18] and the examined porous metal–organic frameworks **MgMOF-74**,[4a,b,10–12] **Cu-TDPAT**,[4c] and **MIL-101** (ref. 13 and 14) are also included. From Fig. 4a, we can see that the highest selectivities are obtained with **MgMOF-74**, **LTA-5A** and **NaX**. Fig. 4b presents the IAST calculations of the $(CO_2 + CH_4)$ uptake capacities. The sum of the component loadings of CO_2 and CH_4 in the mixture is an appropriate measure of the uptake capacity. Examination of the data presented in Fig. 4a and b shows that the *adsorption selectivity* and *uptake capacity* do not go hand-in-hand, especially when the operating pressures, p_t, exceed 1 MPa. For $p_t > 1$ MPa, **LTA-5A** and **NaX** have significantly lower uptake capacities than the four MOFs: **UTSA-40a**, **MgMOF-74**, **Cu-TDPAT**, and **MIL-101**, whereas the adsorption selectivities of both **LTA-5A** and **NaX** are higher than those of **UTSA-40a**, **Cu-TDPAT**, and **MIL-101** in the entire range of pressures. This can be rationalized as follows. **LTA-5A** and **NaX** have pore volumes of 0.25 $cm^3\ g^{-1}$ and 0.28 $cm^3\ g^{-1}$, respectively, significantly lower than those of **UTSA-40a** (0.65 $cm^3\ g^{-1}$), **MgMOF-74** (0.57 $cm^3\ g^{-1}$), **Cu-TDPAT** (0.93 $cm^3\ g^{-1}$), and **MIL-101** (1.38 $cm^3\ g^{-1}$). Therefore, the capacity of **LTA-5A** and **NaX** for $(CO_2 + CH_4)$ uptake becomes limiting for high-pressure operations. Put another way, MOFs with "open" structures are especially attractive for high-pressure separations. **MgMOF-74** is the most unusual MOF because it has a combination of both high selectivities and high capacities. This explains why **MgMOF-74** has excellent separation performance for a wide variety of separation applications.[3c,4a,b,10,20,25]

Breakthrough calculations

The performance of a PSA unit is dictated not only by the adsorption selectivity but also by the capacity to adsorb CO_2 and CH_4. The appropriate combination of the *adsorption selectivity* and *uptake capacity* characteristics is reflected in the breakthrough behaviour in a packed bed adsorber.[26] We therefore performed transient breakthrough calculations following the methodologies developed and described in earlier works.[3c,4c,20,21] Experimental validation of the simulation methodology is provided in earlier works.[3c,f,4c] Fig. 5a shows a schematic diagram of a packed bed adsorber. Fig. 5b presents the molar concentrations of the gas phase exiting the adsorber packed with **UTSA-40a** and maintained under isothermal conditions at 298 K for a 30/20/50 CO_2–CH_4–H_2 ternary mixture operating at a total pressure of 5.0 MPa at the inlet. The *x*-axis is a dimensionless time, τ, obtained by dividing the actual time, t, by the contact time between the gas and the crystallites, $\varepsilon L/u$. Specifically, the calculations presented here were performed taking the following parameter values: $L = 0.1$ m, $\varepsilon = 0.4$, and $u = 0.1$ m s^{-1}. The framework density is 827 kg m^{-3}. From the

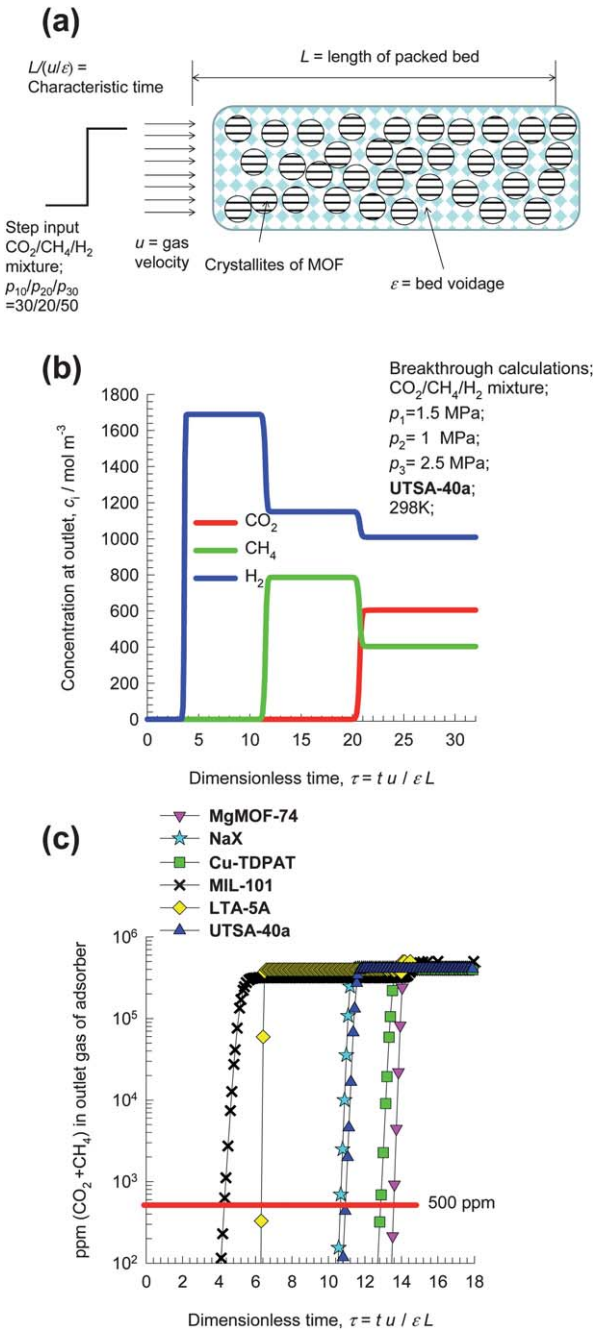

Fig. 5 (a) A schematic diagram of a packed bed adsorber. (b) Breakthrough characteristics of a 30/20/50 CO_2–CH_4–H_2 ternary mixture in an adsorber packed with **UTSA-40a** and maintained under isothermal conditions at 298 K and a total pressure of 5.0 MPa. (c) Ppm $(CO_2 + CH_4)$ in outlet gas as a function of the dimensionless time, τ_{break}, for various adsorbent materials. The total operating pressure is 5.0 MPa.

breakthrough curves, we note that hydrogen breaks through earliest and it is possible to produce pure hydrogen from this 3-component mixture during the adsorption cycle. A comparison of the breakthrough characteristics of different adsorbents operating at the same total pressures of 5.0 MPa is presented in Fig. 5c. When the composition in the exit gas reaches a certain desired purity level, the adsorption cycle needs to be terminated and the contents of the bed regenerated. Longer breakthrough

times are desirable because this reduces the frequency of regeneration. From the gas phase concentrations at the exit of the adsorber, we can determine ppm (CO_2 + CH_4) in outlet gas as a function of the dimensionless time (Fig. 5c). For industrial production of H_2, impurities such as CO_2 and CH_4 need to be reduced to extremely low levels, typically lower than 500 ppm. When this purity level is reached, the corresponding dimensionless breakthrough time, τ_{break}, can be determined, and the amount of 99.95% H_2 produced during the time interval, 0–τ_{break}, can also be obtained according to the material balance across the fixed bed adsorber. Operating at a pressure of 5 MPa, **UTSA-40a** has the longer breakthrough time and the higher production capacity than traditionally used zeolites **NaX** and **LTA-5A** and the examined MOF **MIL-101**.

To demonstrate how the choice of the best material alters with operating pressures, we carried out a series of breakthrough calculations for **UTSA-40a**, **MgMOF-74**, **Cu-TDPAT**, **MIL-101**, **NaX**, and **LTA-5A** for pressures ranging from 0.1 MPa to 6 MPa. Fig. 6a shows the influence of the total operating pressure, p_t, on dimensionless breakthrough time, τ_{break}. The value of τ_{break} decreases for all materials with increasing pressure; this is due to limitations in the capacities with increasing pressure. For a pressure of say 5 MPa, the breakthrough times, τ_{break}, have the following hierarchy: **MgMOF-74** > **Cu-TDPAT** > **UTSA-40a** > **NaX** > **LTA-5A** > **MIL-101**. In other words, the decrease in τ_{break} is a reflection of the approach to pore saturation. The short breakthrough time for **MIL-101** is due to the fact that it has the lowest selectivity. Fig. 6b presents data of the number of moles of 99.95%+ pure H_2 produced per kg of adsorbent material during the time interval, 0–τ_{break}. For pressures exceeding 3 MPa, the hierarchy of productivities is **MgMOF-74** > **Cu-TDPAT** > **UTSA-40a** > **NaX** > **MIL-101** > **LTA-5A**. Furthermore, when the operating pressures are higher than 1 MPa, **UTSA-40a** has a significantly higher productivity than the traditionally used zeolites **NaX** and **LTA-5A**.

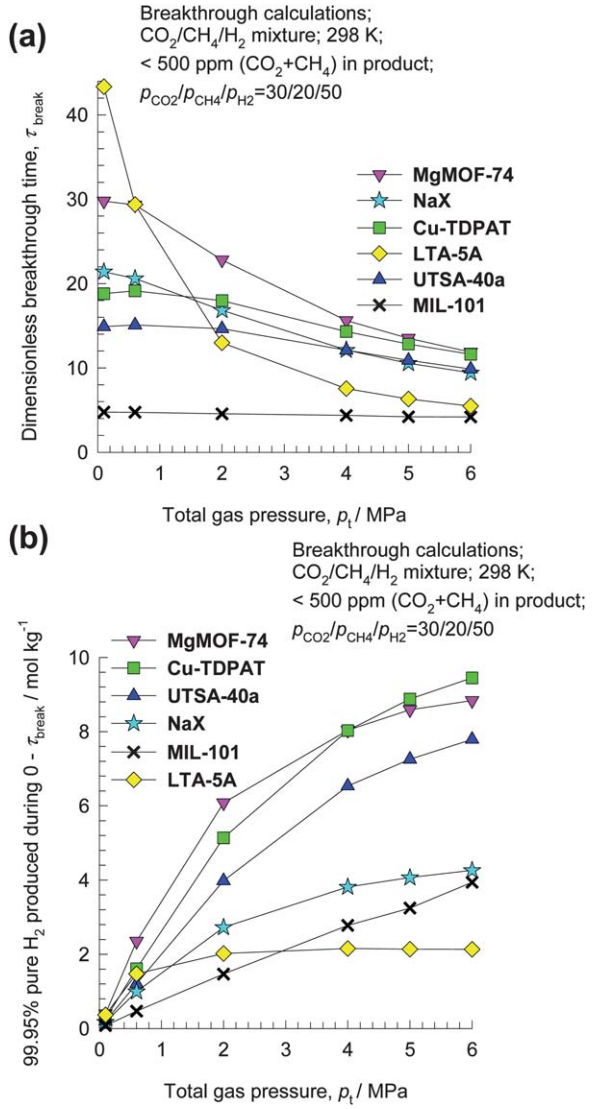

Fig. 6 Influence of the total operating pressure, p_t, on (a) dimensionless breakthrough time, τ_{break}, and (b) the number of moles of 99.95%+ pure H_2 produced per kg of adsorbent material during the time interval, 0–τ_{break}. The breakthrough times, τ_{break}, correspond to those when the outlet gas contains 500 ppm CO_2 + CH_4.

Regeneration of the bed adsorber

The relative costs of regeneration of the bed will be largely dictated by desorption of the CO_2 captured during the time interval, 0–τ_{break}. Let us consider operation at a total pressure of 4 MPa. From a material balance on the adsorber, the amounts of CO_2 captured during the time interval, 0–τ_{break}, are determined to be 4.5, 5.4, 5.7, 3.0, 2.7, and 1.5 mol kg^{-1}, respectively, for **UTSA-40a**, **MgMOF-74**, **Cu-TDPAT**, **MIL-101**, **NaX**, and **LTA-5A**. From the data of the isosteric heats of adsorption (Fig. 7), we can determine the values of $-Q_{st}$ at these CO_2 loadings to be 25, 39.5, 32, 18, 35, and 35 kJ mol^{-1}, respectively. This implies that

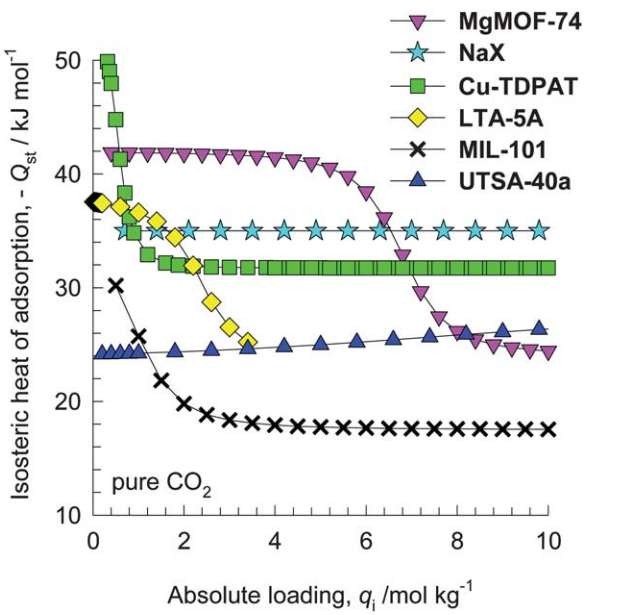

Fig. 7 Comparison of isosteric heats of CO_2 adsorption, Q_{st}, in **UTSA-40a**, **MgMOF-74**, **Cu-TDPAT**, **MIL-101**, **NaX**, and **LTA-5A**. The calculations of Q_{st} are based on the use of the Clausius–Clapeyron equation.

the regeneration requirement of **UTSA-40a** will be significantly lower than that of the traditionally used zeolites **NaX** and **LTA-5A** and the examined MOFs **MgMOF-74** and **Cu-TDPAT** for a desired production of pure H_2.

Conclusions

In summary, we designed and synthesized a novel aromatic-rich tetracarboxylic acid, and incorporated it into a porous metal–organic framework **UTSA-40**. This new porous MOF has a moderately high surface area and suitable pore cages for its high CO_2 and CH_4 adsorption while moderate interactions with CO_2, enabling it as a potential material for high-pressure purification of hydrogen which has been comprehensively examined by simulated breakthrough experiments. The desolvated **UTSA-40a** possesses a higher working capacity and lower regeneration cost when operating at high pressure than the traditionally used zeolites **NaX** and **LTA-5A**. Furthermore, compared with the examined MOFs **MgMOF-74** and **Cu-TDPAT**, the regeneration cost of **UTSA-40a** is significantly lower despite its somewhat lower productivity. The increase of hydrogen productivity can be realized by the optimization of pore surfaces and pore structures; it is expected that some new porous MOFs will be emerging for efficient hydrogen purification with both high productivity and low regeneration cost in the near future.

Acknowledgements

This work was supported by an AX-1730 from Welch Foundation (BC). T.Y. acknowledges support from the DOE BES Grant no. DE-FG02-08ER46522.

Notes and references

1 (*a*) F. V. S. Lopes, C. A. Grande and A. E. Rodrigues, *Chem. Eng. Sci.*, 2011, **66**, 303–317; (*b*) M. Bastos-Neto, A. Moeller, R. Staudt, J. Böhm and R. Gläser, *Chem. Ing. Tech.*, 2011, **83**, 183–190.

2 (*a*) J.-R. Li, J. Sculley and H.-C. Zhou, *Chem. Rev.*, 2012, **112**, 869–932; (*b*) H. Wu, Q. Gong, D. H. Olson and J. Li, *Chem. Rev.*, 2012, **112**, 836–868; (*c*) K. Sumida, D. L. Rogow, J. A. Mason, T. M. McDonald, E. D. Bloch, Z. R. Herm, T.-H. Bae and J. R. Long, *Chem. Rev.*, 2012, **112**, 724–781; (*d*) Y.-S. Bae and R. Q. Snurr, *Angew. Chem., Int. Ed.*, 2011, **50**, 11586–11596; (*e*) S. Kitagawa, R. Kitaura and S.-i. Noro, *Angew. Chem., Int. Ed.*, 2004, **43**, 2334–2375; (*f*) H.-L. Jiang and Q. Xu, *Chem. Commun.*, 2011, **47**, 3351–3370; (*g*) B. Chen, S. Xiang and G. Qian, *Acc. Chem. Res.*, 2010, **43**, 1115–1124; (*h*) Y.-X. Tan, Y.-P. He and J. Zhang, *ChemSusChem*, 2012, **5**, 1597–1601; (*i*) Q. Lin, T. Wu, S.-T. Zheng, X. Bu and P. Feng, *J. Am. Chem. Soc.*, 2012, **134**, 784–787; (*j*) J.-P. Zhang and X.-M. Chen, *J. Am. Chem. Soc.*, 2009, **131**, 5516–5521; (*k*) E. Q. Procopio, F. Linares, C. Montoro, V. Colombo, A. Maspero, E. Barea and J. A. R. Navarro, *Angew. Chem., Int. Ed.*, 2010, **49**, 7308–7311; (*l*) R. Vaidhyanathan, S. S. Iremonger, G. K. H. Shimizu, P. G. Boyd, S. Alavi and T. K. Woo, *Science*, 2010, **330**, 650–653; (*m*) J. An, S. J. Geib and N. L. Rosi, *J. Am. Chem. Soc.*, 2010, **132**, 38–39; (*n*) W.-Y. Gao, W. Yan, R. Cai, K. Williams, A. Salas, L. Wojtas, X. Shi and S. Ma, *Chem. Commun.*, 2012, **48**, 8898–8900; (*o*) Y.-S. Li, F.-Y. Liang, H. Bux, A. Feldhoff, W.-S. Yang and J. Caro, *Angew. Chem., Int. Ed.*, 2010, **49**, 548–551; (*p*) H. Guo, G. Zhu, I. J. Hewitt and S. Qiu, *J. Am. Chem. Soc.*, 2009, **131**, 1646–1647; (*q*) S. Xiang, Y. He, Z. Zhang, H. Wu, W. Zhou, R. Krishna and B. Chen, *Nat. Commun.*, 2012, **3**, 954–962; (*r*) M. C. Das, H. Xu, Z. Wang, G. Srinivas, W. Zhou, Y.-F. Yue, V. N. Nesterov, G. Qian and B. Chen, *Chem. Commun.*, 2011, **47**, 11715–11717; (*s*) Y. He, Z. Zhang, S. Xiang, F. R. Fronczek, R. Krishna and B. Chen, *Chem.–Eur. J.*, 2012, **18**, 613–619; (*t*) M. C. Das, H. Xu, S. Xiang, Z. Zhang, H. D. Arman, G. Qian and B. Chen, *Chem.–Eur. J.*, 2011, **17**, 7817–7822; (*u*) H. Xu, Y. He, Z. Zhang, S. Xiang, J. Cai, Y. Cui, Y. Yang, G. Qian and B. Chen, *J. Mater. Chem. A*, 2013, **1**, 77–81.

3 (*a*) S. Xiang, Z. Zhang, C.-G. Zhao, K. Hong, X. Zhao, D.-L. Ding, M.-H. Xie, C.-D. Wu, R. Gill, K. M. Thomas and B. Chen, *Nat. Commun.*, 2012, **2**, 204; (*b*) M. C. Das, Q. Guo, Y. He, J. Kim, J. C.-G. Zhao, K. Hong, S. Xiang, Z. Zhang, K. M. Thomas, R. Krishna and B. Chen, *J. Am. Chem. Soc.*, 2012, **134**, 8703–8710; (*c*) Y. He, R. Krishna and B. Chen, *Energy Environ. Sci.*, 2012, **5**, 9107–9120; (*d*) Y. He, W. Zhou, R. Krishna and B. Chen, *Chem. Commun.*, 2012, **48**, 11813–11831; (*e*) Y.-S. Bae, C. Y. Lee, K. C. Kim, O. K. Farha, P. Nickias, J. T. Hupp, S. T. Nguyen and R. Q. Snurr, *Angew. Chem., Int. Ed.*, 2012, **51**, 1857–1860; (*f*) E. D. Bloch, W. L. Queen, R. Krishna, J. M. Zadrozny, C. M. Brown and J. R. Long, *Science*, 2012, **335**, 1606–1610; (*g*) Z. Zhang, S. Xiang and B. Chen, *CrystEngComm*, 2011, **13**, 5983–5992.

4 (*a*) Z. R. Herm, J. A. Swisher, B. Smit, R. Krishna and J. R. Long, *J. Am. Chem. Soc.*, 2011, **133**, 5664–5667; (*b*) Z. R. Herm, R. Krishna and J. R. Long, *Microporous Mesoporous Mater.*, 2012, **157**, 94–100; (*c*) H. Wu, K. Yao, Y. Zhu, B. Li, Z. Shi, R. Krishna and J. Li, *J. Phys. Chem. C*, 2012, **116**, 16609–16618.

5 (*a*) O. K. Farha, A. Ö. Yazaydın, I. Eryazici, C. D. Malliakas, B. G. Hauser, M. G. Kanatzidis, S. T. Nguyen, R. Q. Snurr and J. T. Hupp, *Nat. Chem.*, 2010, **2**, 944–948; (*b*) D. Yuan, D. Zhao, D. Sun and H.-C. Zhou, *Angew. Chem., Int. Ed.*, 2010, **49**, 5357–5361; (*c*) Y. Yan, I. Telepeni, S. Yang, X. Lin, W. Kockelmann, A. Dailly, A. J. Blake, W. Lewis, G. S. Walker, D. R. Allan, S. A. Barnett, N. R. Champness and M. Schröder, *J. Am. Chem. Soc.*, 2010, **132**, 4092–4094; (*d*) L. Ma, D. J. Mihalcik and W. Lin, *J. Am. Chem. Soc.*, 2009, **131**, 4610–4612; (*e*) Y. He, Z. Zhang, S. Xiang, H. Wu, F. R. Fronczek, W. Zhou, R. Krishna, M. O'Keeffe and B. Chen, *Chem.–Eur. J.*, 2012, **18**, 1901–1904; (*f*) Z. Guo, H. Wu, G. Srinivas, Y. Zhou, S. Xiang, Z. Chen, Y. Yang, W. Zhou, M. O'Keeffe and B. Chen, *Angew. Chem., Int. Ed.*, 2011, **50**, 3178–3181; (*g*) B. Zheng, J. Bai, J. Duan, L. Wojtas and M. J. Zaworotko, *J. Am. Chem. Soc.*, 2011, **133**, 748–751; (*h*) B. Li, Z. Zhang, Y. Li, K. Yao, Y. Zhu, Z. Deng, F. Yang, X. Zhou, G. Li, H. Wu, N. Nijem, Y. J. Chabal, Z. Lai,

Y. Han, Z. Shi, S. Feng and J. Li, *Angew. Chem., Int. Ed.*, 2012, **51**, 1412–1415; (*i*) X. Zhao, D. Sun, S. Yuan, S. Feng, R. Cao, D. Yuan, S. Wang, J. Dou and D. Sun, *Inorg. Chem.*, 2012, **51**, 10350–10355.

6 (*a*) B. Chen, N. W. Ockwig, A. R. Millward, D. S. Contreras and O. M. Yaghi, *Angew. Chem., Int. Ed.*, 2005, **44**, 4745–4749; (*b*) X. Lin, J. Jia, X. Zhao, K. M. Thomas, A. J. Blake, G. S. Walker, N. R. Champness, P. Hubberstey and M. Schröder, *Angew. Chem., Int. Ed.*, 2006, **45**, 7358–7364; (*c*) Y.-G. Lee, H. R. Moon, Y. E. Cheon and M. P. Suh, *Angew. Chem., Int. Ed.*, 2008, **47**, 7741–7745; (*d*) M. Xue, G. Zhu, Y. Li, X. Zhao, Z. Jin, E. Kang and S. Qiu, *Cryst. Growth Des.*, 2008, **8**, 2478–2483; (*e*) X.-S. Wang, S. Ma, K. Rauch, J. M. Simmons, D. Yuan, X. Wang, T. Yildirim, W. C. Cole, J. J. López, A. d. Meijere and H.-C. Zhou, *Chem. Mater.*, 2008, **20**, 3145–3152; (*f*) Y. Hu, S. Xiang, W. Zhang, Z. Zhang, L. Wang, J. Bai and B. Chen, *Chem. Commun.*, 2009, 7551–7553; (*g*) D. Zhao, D. Yuan, A. Yakovenko and H.-C. Zhou, *Chem. Commun.*, 2010, **46**, 4196–4198; (*h*) X. Lin, I. Telepeni, A. J. Blake, A. Dailly, C. M. Brown, J. M. Simmons, M. Zoppi, G. S. Walker, K. M. Thomas, T. J. Mays, P. Hubberstey, N. R. Champness and M. Schröder, *J. Am. Chem. Soc.*, 2009, **131**, 2159–2171; (*i*) S. Ma, D. Sun, J. M. Simmons, C. D. Collier, D. Yuan and H.-C. Zhou, *J. Am. Chem. Soc.*, 2008, **130**, 1012–1016.

7 Y. He, C.-G. Zhao and B. Chen, unpublished results.

8 W. Zhou, H. Wu, M. R. Hartman and T. Yildirim, *J. Phys. Chem. C*, 2007, **111**, 16131–16137.

9 A. L. Spek, *PLATON*, The University of Utrecht, Utrecht, The Netherlands, 1999.

10 J. A. Mason, K. Sumida, Z. R. Herm, R. Krishna and J. R. Long, *Energy Environ. Sci.*, 2011, **4**, 3030–3040.

11 P. D. C. Dietzel, V. Besikiotis and R. Blom, *J. Mater. Chem.*, 2009, **19**, 7362–7370.

12 www.hydrogen.energy.gov/pdfs/review11/st049_yaghi_2011_p.pdf.

13 P. Chowdhury, S. Mekala, F. Dreisbach and S. Gumma, *Microporous Mesoporous Mater.*, 2012, **152**, 246–252.

14 M. Latroche, S. Surblé, C. Serre, C. Mellot-Draznieks, P. L. Llewellyn, J.-H. Lee, J.-S. Chang, S. H. Jhung and G. Férey, *Angew. Chem., Int. Ed.*, 2006, **45**, 8227–8231.

15 Y. Belmabkhout, G. Pirngruber, E. Jolimaitre and A. Methivier, *Adsorption*, 2007, **13**, 341–349.

16 S. Cavenati, C. A. Grande and A. E. Rodrigues, *J. Chem. Eng. Data*, 2004, **49**, 1095–1101.

17 S. Pakseresht, M. Kazemeini and M. M. Akbarnejad, *Sep. Purif. Technol.*, 2002, **28**, 53–60.

18 S. Sircar and T. C. Golden, *Sep. Sci. Technol.*, 2000, **35**, 667–687.

19 A. L. Myers and J. M. Prausnitz, *AIChE J.*, 1965, **11**, 121–127.

20 R. Krishna and J. M. van Baten, *J. Membr. Sci.*, 2011, **377**, 249–260.

21 R. Krishna and R. Baur, *Sep. Purif. Technol.*, 2003, **33**, 213–254.

22 R. Krishna, S. Calero and B. Smit, *Chem. Eng. J.*, 2002, **88**, 81–94.

23 R. Krishna and J. M. van Baten, *Chem. Eng. J.*, 2007, **133**, 121–131.

24 R. Krishna and J. M. van Baten, *Phys. Chem. Chem. Phys.*, 2011, **13**, 10593–10616.

25 R. Krishna, *Microporous Mesoporous Mater.*, 2012, **156**, 217–223.

26 R. Krishna and J. R. Long, *J. Phys. Chem. C*, 2011, **115**, 12941–12950.